

Heterodyne Holography with full control of both signal and reference arms

Michel Gross¹

¹Laboratoire Charles Coulomb (L2C), UMR 5221 CNRS-Université de Montpellier, Montpellier, F-France*

Heterodyne holography is a variant of phase shifting holography in which reference and signal arms are controlled by acousto optic modulators. In this review paper, we will briefly describe the method and its properties, and we will illustrate its advantages in experimental applications.

Ocis : 090.1995 : Holography : Digital holography ;
040.2840 : Detectors-Heterodyne.

Citation : Michel Gross, Heterodyne holography with full control of both the signal and reference arms, *Appl. Opt.* **55**, pA8–A16 (2016) doi : 10.1364/AO.55.0000A8
<https://www.osapublishing.org/ao/abstract.cfm?uri=ao-55-~^~^>

I. INTRODUCTION

Heterodyne holography [1, 2] is a technique firstly introduced 15 years ago realized by modifying a phase shifting holography setup [3]. The main advantage of heterodyne holography is that the frequency, phase and amplitude of both reference and signal arms are controlled by acousto optic modulators (AOM). By shifting the frequency ω_{LO} of the reference beam, called here local oscillator, with respect to the frequency ω_I of illumination, heterodyne holography is able to detect the light scattered by the object at any frequency ω close to ω_{LO} , which can be equal or different than the frequency ω_I of illumination of the object.

If the light is scattered by the object over a broad continuous frequency spectrum, heterodyne holography must be combined with off-axis holography in order to separate the images corresponding to the +1 and -1 holographic grating orders. Indeed, in that case, the +1 and -1 holographic images are both non-zero, since they correspond to the detection of signals at frequencies that are different but very close and within the object broad frequency spectrum [9]. This point will be discussed in section II C. Heterodyne holography in off axis configuration has been used since 2003 [4].

Heterodyne holography performs heterodyne detection with a slow 2D multi pixels detector (CCD or CMOS camera). The bandwidth BW of the detection is narrow (10 to 1000 Hz depending on the camera), but the beat frequency $\omega - \omega_{LO}$ can be large (up to several MHz [4]). Heterodyne holography must be distinguished from optical scanning holography that uses a fast mono pixel detector (photodiode), and that makes mechanical scans along the x and y axis to get holograms [5].

We will briefly describe the heterodyne holographic technique and illustrate its advantages on experimental examples.

II. PRINCIPLE AND PROPERTIES OF HETERODYNE HOLOGRAPHY

A. Typical setup

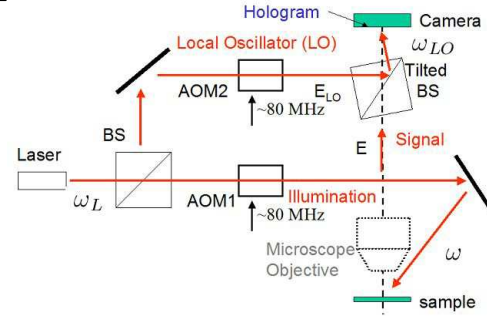


FIGURE 1. Typical heterodyne holography setup in transmission geometry. BS : beam splitter; AOM1, AOM2 : acousto-optic modulators; E_{LO} and E : reference (i.e. local oscillator LO) and object fields whose optical frequencies are ω_{LO} and ω ; $\omega_{AOM1/2}$: driving frequencies ($\simeq 80$ MHz) of the acousto optics modulators AOM1 and AOM2.

Figure 1 shows a typical heterodyne holography setup. The frequency and the amplitude of both the illumination and the reference arms are controlled by the two acousto optics modulator (Bragg cells) AOM1 and AOM2. AOM1, which is driven by a Radio Frequency (RF) signals at ω_{AOM1} (with $\omega_{AOM1} \simeq 80$ MHz), shifts the frequency ω_I of illumination so that

$$\omega_I = \omega_L + \omega_{AOM1} \quad (1)$$

where ω_L is the optical frequency of the main laser. Similarly AOM2 shift the frequency ω_{LO} of the local oscillator arm so that

$$\omega_{LO} = \omega_L + \omega_{AOM2} \quad (2)$$

An angularly tilted beam splitter BS mixes the signal field scattered by the sample $\mathcal{E}(t) = E e^{j\omega t}$ and reference field $\mathcal{E}_{LO}(t) = E_{LO} e^{j\omega_{LO} t}$. Thus, the interference pattern I that is recorded by the CCD camera is :

$$I(t) = |\mathcal{E}(t) + \mathcal{E}_{LO}(t)|^2 \quad (3)$$

$$= |E|^2 + |E_{LO}|^2 + EE_{LO}^* e^{-j(\omega_{LO}-\omega)t} + \text{c.c.}$$

where c.c. is the complex conjugate of the EE_{LO}^* term i.e. $\text{c.c.} = E^* E_{LO} e^{+j(\omega_{LO}-\omega)t}$. Sequence of frames I_n

* michel.gross@univ-montp2.fr

are recorded by the camera, with :

$$\begin{aligned}
 I_n &= \frac{1}{T} \int_{t=nT_{CCD}-T/2}^{nT_{CCD}+T/2} dt |\mathcal{E}(t) + \mathcal{E}_{LO}(t)|^2 \\
 &= |E|^2 + |E_{LO}|^2 \\
 &\quad + EE_{LO}^* \left[\frac{1}{T} \int_{t=nT_{CCD}-T/2}^{nT_{CCD}+T/2} dt e^{-j(\omega_{LO}-\omega)t} \right] + \text{c.c.} \\
 &= |E|^2 + |E_{LO}|^2 \\
 &\quad + EE_{LO}^* \text{sinc}((\omega - \omega_{LO})T/2) e^{-j(\omega_{LO}-\omega)t_n} + \text{c.c.}
 \end{aligned} \tag{4}$$

where $t_n = nT_{CCD}$ with n integer, $T_{CCD} = 2\pi/\omega_{CCD}$, and $\omega_{CCD}/2\pi$ is the camera frame frequency. The sinc factor of Eq. 4 corresponds to the integration of the beat signal of frequency $\omega_{LO} - \omega$ over the camera exposure time T .

Note that a microscope objective can added to the setup to perform heterodyne holographic microscopy [6–8].

B. Different number of frames detection

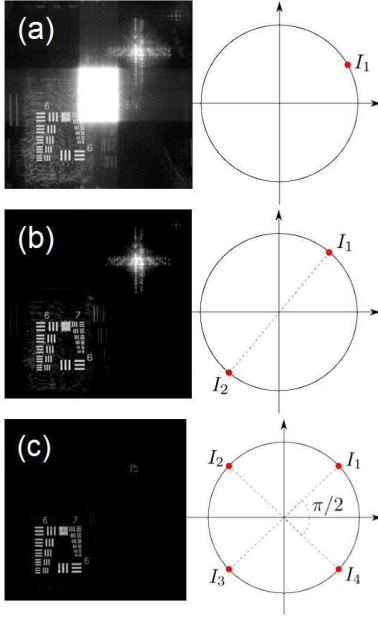


FIGURE 2. (Left hand side) Reconstructed images of a USAF target obtained with 1 frame (a), 2 frames (b) and 4 frames (c) heterodyne holography. (Right hand side) Phase of the signal field E (relative to E_{LO}) for the successive frames $I_1, I_2 \dots$ of the sequence.

Different types of holographic detection schemes can be implemented with the setup of Fig. 1. To illustrate this point, we have considered a USAF target sample. Since the target does not move, the light is scattered by the target at the illumination frequency $\omega = \omega_I$.

1. One frame off axis holography

One frame off axis holography is made by choosing $\omega_{AOM2} = \omega_{AOM1}$ (so that $\omega_{LO} = \omega_I = \omega$), and $H = I_1$ for the hologram. We get then :

$$\begin{aligned}
 H = I_1 &= |E|^2 + |E_{LO}|^2 \\
 &\quad + \text{sinc}((\omega - \omega_{LO})T/2)(EE_{LO}^* + E^*E_{LO})
 \end{aligned} \tag{5}$$

Figure 2 (a) shows the reconstructed image obtained in that case. The image exhibits 3 bright zones. The bright square in the center of the reconstructed image is the zero grating order. It corresponds to the $|E_{LO}|^2 + |E|^2$ terms. The blurred bright zone in the upper right side of the image is the -1 grating order. It corresponds to $E_{LO}E^*$. Lastly, the USAF image that is sharp in the lower left side of the reconstructed image is the $+1$ grating order that corresponds to E_{LO}^*E .

2. Two frames phase shifting holography

Phases shifting holography with 2 frames is made by tuning the local oscillator frequency to have $\omega_{AOM2} - \omega_{AOM1} = \omega_{CCD}/2$ (so that $\omega_{LO} - \omega_I = \omega_{CCD}/2$). For detection at the illumination frequency (i.e. for $\omega = \omega_I$), the phase factor $e^{-j(\omega_{LO}-\omega)t_n}$ of Eq. 4 becomes thus equal to -1^{n-1} . We get for I_1 and I_2 :

$$\begin{aligned}
 I_1 &= |E|^2 + |E_{LO}|^2 \\
 &\quad + \text{sinc}((\omega - \omega_{LO})T/2)(EE_{LO}^* + E^*E_{LO}) \\
 I_2 &= |E|^2 + |E_{LO}|^2 \\
 &\quad + \text{sinc}((\omega - \omega_{LO})T/2)(-EE_{LO}^* - E^*E_{LO})
 \end{aligned} \tag{6}$$

By choosing $H = I_1 - I_2$, we get :

$$\begin{aligned}
 H &= I_1 - I_2 \\
 &= 2 \text{sinc}((\omega - \omega_{LO})T/2)(EE_{LO}^* + E^*E_{LO})
 \end{aligned} \tag{7}$$

Figure 2 (b) shows the 2 frames reconstructed image. This image exhibits only 2 bright zones, which correspond to the orders $+1$ and -1 i.e. to EE_{LO}^* and E^*E_{LO} .

3. Four frames phase shifting holography

Four phases phase shifting holography is made with $\omega_{AOM2} - \omega_{AOM1} = \omega_{CCD}/4$ so that $\omega_{LO} = \omega_I + \omega_{CCD}/4$. For $t = t_n$, the phase factor $e^{-j(\omega_{LO}-\omega)t}$ is thus equal to $(-j)^{n-1}$. We get :

$$\begin{aligned}
 I_1 &= |E|^2 + |E_{LO}|^2 \\
 &\quad + \text{sinc}((\omega - \omega_{LO})T/2)(EE_{LO}^* + E^*E_{LO}) \\
 I_2 &= |E|^2 + |E_{LO}|^2 \\
 &\quad + \text{sinc}((\omega - \omega_{LO})T/2)(-jEE_{LO}^* + jE^*E_{LO}) \\
 I_3 &= |E|^2 + |E_{LO}|^2 \\
 &\quad + \text{sinc}((\omega - \omega_{LO})T/2)(-EE_{LO}^* - E^*E_{LO}) \\
 I_4 &= |E|^2 + |E_{LO}|^2 \\
 &\quad + \text{sinc}((\omega - \omega_{LO})T/2)(+jEE_{LO}^* - jE^*E_{LO})
 \end{aligned} \tag{8}$$

By choosing $H = (I_1 - I_3) + j(I_2 - I_4)$, we get :

$$\begin{aligned} H &= (I_1 - I_3) + j(I_2 - I_4) \\ &= 4 \text{sinc}((\omega - \omega_{LO}T/2))EE_{LO}^* \end{aligned} \quad (9)$$

Figure 2 (c) shows the 4 frames reconstructed image. This image exhibits only the +1 grating order EE_{LO}^* , which gives a sharp image of the USAF target.

C. Frequency response $\eta(\omega)$ of the holographic heterodyne detection

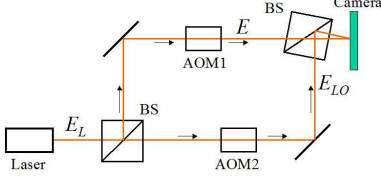


FIGURE 3. Setup of the holographic experiment used to measure the frequency response $\eta(\omega)$. BS : beam splitter; AOM1, AOM2 : acousto-optic modulators; E_{LO} and E : reference (i.e. local oscillator LO) and object fields whose optical frequencies are ω_{LO} and ω

In the USAF target experiment, the position of the sample do not change and the light is scattered at the illumination frequency $\omega = \omega_I$. In some other cases, the sample could be moved and the frequency of the scattered light can be Doppler shifted. Thus, it is important to know the frequency response $\eta(\omega)$ of the holographic heterodyne detection.

To determine η an holographic control experiment illustrated by Fig. 3 has been performed [9]. The experiment is made by recording sequence of frames I_n for different frequency $\omega = \omega_I$ of the object beam, the LO beam frequency ω_{LO} being kept constant. The four phases hologram H is calculated and the +1 grating order signal EE_{LO}^* is selected in the Fourier space [10].

For each signal frequency ω , a sequence of frames I_n is recorded, and four phases holograms H and \tilde{H} are calculated in real and Fourier space :

$$\begin{aligned} H(x, y) &= (I_1(x, y) - I_3(x, y)) \\ &\quad + j(I_2(x, y) - I_4(x, y)) \end{aligned} \quad (10)$$

$$\tilde{H}(k_x, k_y) = \text{FFT}[H(x, y)]$$

where FFT is the 2D Fourier transform operator.

Figure 4 (a) displays $|\tilde{H}|^2$ that is obtained with $\omega_{AOM2} - \omega_{AOM1} = +\omega_{CCD}/4$. The brighter point on the left (within circle 1) corresponds to the +1 grating order signal $|EE_{LO}^*|^2$, while the point on the right (within circle 2) is the -1 grating order signal $|E^*E_{LO}|^2$, whose intensity is much lower. Here in Fig. 4 (a), the 4 phase detection made with $\omega_{LO} - \omega = +\omega_{CCD}/4$, allows one to select the +1 grating order and to reject the -1 order.

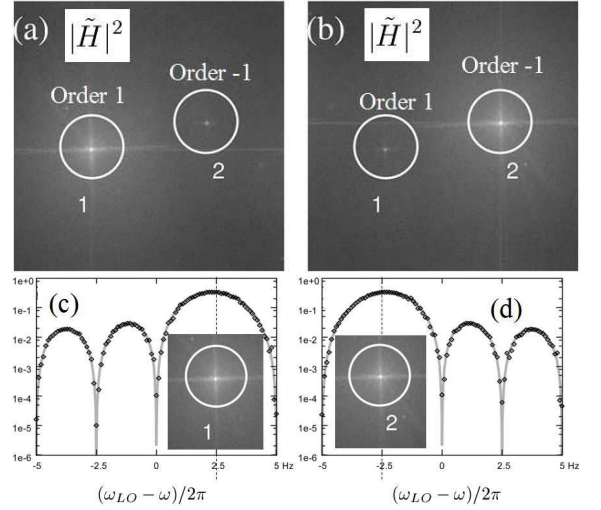


FIGURE 4. (a,b) Fourier space holograms $|\tilde{H}|^2$ obtained with $\omega_{AOM2} - \omega_{AOM1} = +\omega_{CCD}/4$ (a) and $-\omega_{CCD}/4$ (b) with $\omega_{CCD}/2\pi = 10$ Hz. Weights $W_{\pm 1}$ of the signal $|H|^2$ summed over regions 1 and 2 of Fig 4 (a) and (b) are plotted in (c,d). W_{+1} is plotted in (c), W_{-1} in (d). Horizontal axis is $(\omega_{LO} - \omega)/2\pi$. Points are measurements : $W_{\pm 1}$ given by Eq. 11, solid gray line is theory : $|\eta|^2$ given by Eq. 13 [9].

In figure 4 (b), in contrast, with $\omega_{LO} - \omega = -\omega_{CCD}/4$ one selects the -1 grating order and rejects the +1 order, since the -1 image is bright, while the +1 image is dark.

We have measured the weight of the ± 1 signals $W_{\pm 1}$ defined by

$$W_{\pm 1} = \sum_{\pm 1} |\tilde{H}(k_x, k_y)|^2 \quad (11)$$

where $\sum_{\pm 1}$ is the sum over a 10×10 pixel region centered on the ± 1 peaks. By sweeping the AOM1 frequency, we have studied how $W_{\pm 1}$ varies with ω . Figure 4 (c,d) shows $W_{\pm 1}$ as a function of $\omega_{LO} - \omega$. When the four-phase condition is fulfilled, i.e., when $\omega_{LO} - \omega = +\omega_{CCD}/4$, the weight W_{+1} of +1 signal is maximum (i.e. $W_{+1} \sim 1$) and the twin signal is nearly zero (i.e. $W_{-1} \sim 10^{-4}$). Conversely, when $\omega_{LO} - \omega = -\omega_{CCD}/4$, W_{-1} is large and W_{+1} nearly zero.

The weight W_{+1} of $|EE_{LO}^*|^2$ term is proportional to $|\eta|^2$, where η is the EE_{LO}^* detection efficiency. For four phases detection with $4N$ frames i.e. for

$$H = (1/4N) \sum_{n=1}^{4N} j^{n-1} I_n \quad (12)$$

we have [11] :

$$\begin{aligned} \eta(x) &= \frac{1}{4NT} \sum_{n=0}^{4N-1} j^n \int_{t=nT_{CCD}-T/2}^{nT_{CCD}+T/2} e^{2\pi x t} dt \\ &= \text{sinc}(\pi x T) \times \frac{1}{4N} \sum_{n=0}^{4N-1} j^n e^{2\pi n x T_{CCD}} \end{aligned} \quad (13)$$

where $x = (\omega - \omega_{LO})/2\pi$ is the heterodyne beat frequency in Hz, T the frame exposure time and $T_{CCD} = 2\pi/\omega_{CCD}$ the frame to frame time.

In Eq. 13, the factor $\text{sinc}(\pi x T)$, which has been already introduced in Eq. 4, corresponds to the integration of the beat signal, whose frequency is non-zero, over the camera exposure time T . Because of Eq. 12, the summation over the $4N$ frames of Eq. 13 is made with a phase factor j^n . To the end, the factor $1/4N$ is a normalization factor that is the inverse of the number of terms within the summation. With this normalization factor the maximum of $|\eta(x)|$ is slightly lower than 1.

As depicted in Fig. 4 (c), the experimental results for $W_{\pm 1}$ (points) agree with $|\eta|^2$, where η is given by Eq. 13 with $T = T_{CCD} = 0.1$ s and $4N = 4$ (solid gray curves). This means that heterodyne holography is able to perform phase shifting with very accurate phase [9]. The hologram H can thus be calculated without having to take account for the phase errors of the experimental setup.

We must notice also that the $+1$ grating order image corresponds to the $\omega_{LO} + \omega_{CCD}/4$ signal, while the -1 image corresponds to $\omega_{LO} - \omega_{CCD}/4$. If the frequency spectrum of the signal field E is broad and cover both $\omega_{LO} \pm \omega_{CCD}/4$ frequency components, the ± 1 images both exist. One must thus work off axis in order to separate them, and to avoid image alias.

The purpose of Fig. 4 experiment is to measure the frequency response of the holographic detection. It turns out that the detection bandwidth BW (that is the width of the frequency response) is very narrow (about ± 2.5 Hz). It is nevertheless possible to detect signals with Doppler shift or Doppler broadening much larger than BW. Indeed, Fig. 4 shows also that the detection is made at a frequency close to ω_{LO} with an offset of $+ 2.5$ Hz. By changing the frequency ω_{LO} it is thus possible to tune the holographic detection at any wanted frequency. In [4] for example, the signal is an ultrasonic sideband whose frequency ω is shifted by 2.2 MHz with respect to the object illumination frequency ($\omega \simeq \omega_I + 2.2$ MHz). This sideband signal has been detected by tuning ω_{LO} near ω , the best detection efficiency being obtained with $\omega_{LO} = \omega + \omega_{CCD}/4$.

D. Bandwidth BW of the holographic heterodyne detection

The bandwidth BW of the holographic heterodyne detection depends on the acquisition condition, in particular on the total exposure time. To illustrate this point, we have plotted, for four phases detection with $4N$ frames, the detection efficiency $|\eta(x)|^2$ given by Eq. 13.

As shown in Fig. 5, the detection bandwidth BW (i.e. the width of the frequency response $|\eta(x)|^2$) is inversely proportional to the exposure time : $\text{BW} = (4T)^{-1}$, $(8T)^{-1}$ and $(16T)^{-1}$ for 4, 8 and 16 frames respectively. This illustrates the coherent character of the detection.

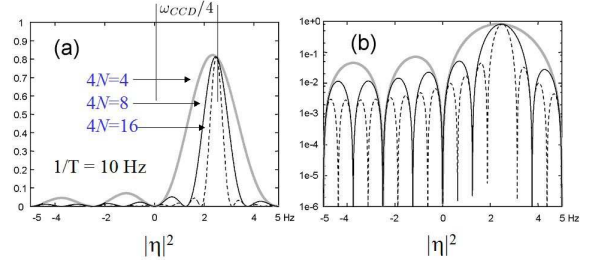


FIGURE 5. Detection efficiency $|\eta|^2$ for four phases heterodyne detection with $4N$ frames : $4N = 4$ (heavy grey line), $4N = 8$ (solid black line), and $4N = 16$ (dashed black line). Calculation is done for $T = T_{CCD} = 0.1$ s. Vertical axis axis is $|\eta|^2$ in linear (a) and logarithmic (b) scales. Horizontal axis is $(\omega_{LO} - \omega)/2\pi$ in Hz

E. Double filtering of the zero order signal and shot noise

Since laser emission and photodetection on a camera pixel are random processes, the signal I that is detected on each pixel exhibits shot noise. This noise is gaussian and its standard deviation σ is equal to \sqrt{I} , where I is the pixel signal expressed in photo electron Units (e). When performing heterodyne holography in dim light condition i.e. when $|E| \ll |E_{LO}|$ the detection sensitivity is generally limited by the shot noise on the local oscillator, since $I \simeq |E_{LO}|^2$.

To illustrate this point let us consider an example. Digital holography is made with an 8 bits camera, whose full well capacity is $2 \cdot 10^4 e$. The camera signal I varies from 0 to 255 Digital Counts (DC) and the camera "gain" is $G = 78 e/\text{DC}$. In a typical situation, the local oscillator is adjusted to half saturation, and the local oscillator is $|E_{LO}|^2 = 10^4 e = 128 \text{ DC}$.

The shot noise, whose standard deviation is $\sigma = \sqrt{I} = 100 e$, is much larger than the camera read noise ($\sigma < 30 e$), and than the quantization noise of the camera Analog Digital converter ($\sigma = 78/\sqrt{12} = 6.5 e$). On the other hand, the shot noise equivalent signal is $1 e$ per pixel. Indeed, if we consider a very low signal : $|E|^2 = 1 e$, the $+1$ grating order holographic term $|EE_{LO}^*| = 100 e$ is equal to the shot noise variance $\sigma = 100 e$.

This result, which is valid for 1 frame, remains valid whatever the number of frames $4N$ is. Indeed, shot noise is a broadband white noise. The noise that is detected is thus proportional to the product of the total exposure time $4NT$ with the detection bandwidth BW, which is proportional to $(4NT)^{-1}$. The shot noise equivalent signal does not depend on the number of frames $4N$. The shot noise is thus always equal to $1 e$ per pixel.

So, at this point a question arose : how it is possible to reach this shot noise limit in real time holographic experiment ? As discussed above, the read noise and the quantization noise are lower than shot noise. The last extra noise that must be considered is the technical noise

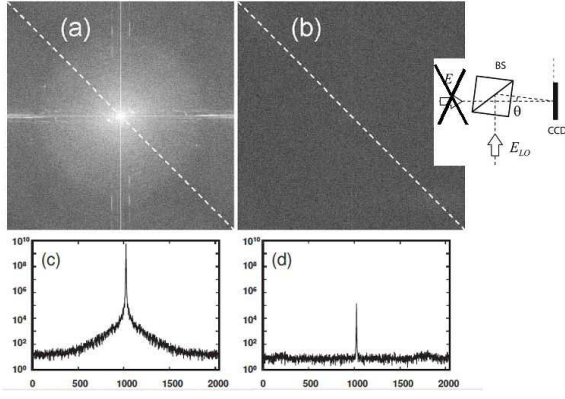


FIGURE 6. (a,b) Images of the Fourier holograms \tilde{H}^2 obtained without signal (i.e. with $|E|^2 = 0$). (c,d) Cut along the white dashed diagonal lines of the (a,b) images. Vertical axis is \tilde{H}^2 along the cut averaged over 11 pixels : \tilde{H}^2 is plotted in log scale. Horizontal axis is the pixel index (0...2047) along the k_x and k_y axis of the Fourier space. The 1280×1024 recorded hologram is padded into 2048×2048 calculation grid. The Fourier space is thus 2048×2048 pixels, whose size is $2\pi/(2048D_{pix})$, where $D_{pix} = 6.7\mu\text{m}$ is the camera pixel size. Images and cut are calculated with one frame (a,c) and four frames holograms (b,d). See [12].

on the LO beam, because the LO signal is dominant since $|E_{LO}|^2 \gg |E|^2$. This technical noise is the sum of the noises that differ from shot noise and that affect the LO beam signal. The noise on the power supply of main laser, the vibration of the setup, or the noise on the AOMs or on the RF signal that drives the AOMs contribute to technical noise. Whatever its origin, the LO technical noise is highly correlated from pixel to the next, since the LO beam that reaches the camera is flat field ($|E_{LO}|^2$ varies slowly with position x and y).

It is thus possible to reach the shot noise limit by filtering the LO technical noise. A control holographic experiment made without signal (i.e. with $|E|^2 = 0$) illustrates this filtering [12]. Figure 6(a, b) shows the Fourier space holograms $|\tilde{H}|^2$ that are obtained with one (a) and four frames (b). With one frame (a) i.e. with $H = I_1$, the LO signal $|\tilde{H}|^2$, which is located in the center of the calculation grid, is brighter and extends over a larger area than with four frames i.e. with $H = (I_1 - I_3) + j(I_2 - I_4)$ (b).

To make a quantitative analysis of these images, we have plotted, on Figs. 6 (c) and (d), $|\tilde{H}(k_x, k_y)|^2$ along the diagonal dashed lines of Figs. 6 (a) and (b) respectively. We have made diagonal cuts in order to explore zones of the Fourier space that are far from regions with k_x or $k_y \simeq 0$ where the Fast Fourier Transform (FFT) alias can be observed as in Fig. 6(a). For $k_x = k_y = 0$, we obtain a peak on the Figs. 6 (c) and (d) cuts. These peaks corresponds to the LO field $|E_{LO}|^2$.

In the one frame case (Fig. 6 (c)), the peak is much larger and much broader, than in the four frames case (Fig. 6 (d)). It results that most of the Fourier space is

polluted by the one frame LO parasitic signal, which is several orders of magnitude larger than its four frames counterpart. The one frame LO parasitic signal is much larger than the shot-noise limit, which is equal, within a few percent as experimentally verified, to the four frames noise floor seen on Fig. 6 (d).

Here, in the control holographic experiment made without signal, the shot-noise limit can be reached with four frames detection, because the LO signal $|E_{LO}|^2$ (and the LO technical noise) are filtered off by a double filtering procedure in space and time.

- Filtering in space is made by selecting, in the Fourier space, the off axis region where the $+1$ grating order signal EE_{LO}^* is located. This region is far from the center of the Fourier space (see for example Fig. 2 (a)), where the LO beam signal $|E_{LO}|^2$ is located.
- Filtering in time is made by the demodulation equation $H = (I_1 - I_3) + j(I_2 - I_4)$, which calculate H from difference of frames recorded at different times. Since $|E_{LO}|^2$ does not vary with time, $|E_{LO}|^2$ is filter off by the demodulation equation, as seen on Eq. 9.

III. HETERODYNE HOLOGRAPHY EXAMPLES OF EXPERIMENTS

To illustrate the advantages of heterodyne holography, we will present here two examples of experiment.

A. Sideband holography

The main advantage of heterodyne holography is its ability to detect the holographic signal at a frequency that is different from that of illumination. To illustrate this point, we will first consider the detection of the light scattered by a vibrating object.

1. Optical signal scattered by a vibrating object

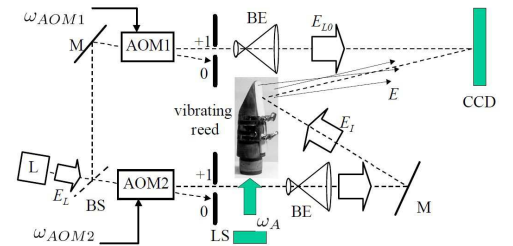


FIGURE 7. Heterodyne holography setup applied to analyse vibration of a clarinet reed. L : main laser; AOM1, AOM2 : acousto-optic modulators; M : mirror; BS : beam splitter; BE : beam expander; CCD : camera; LS : loud-speaker exciting the vibrating clarinet reed at frequency $\omega_A/2\pi$.

Figure 7 shows a typical example of vibration holographic experiment setup in reflection geometry. The object is a clarinet reed, whose vibration is excited by a loudspeaker LS. The vibration is studied by heterodyne holography with a reference local oscillator beam (field E_{LO}) that can be frequency shifted with respect to the illumination beam (field E_I).

Let us consider that the objet (the clarinet reed) that vibrates at frequency ω_A with amplitude z_{max} . The displacement z along the out of plane direction is

$$z(t) = z_{max} \sin \omega_A t \quad (14)$$

In backscattering geometry, this corresponds to a phase modulation $\varphi(t)$ of the signal :

$$\begin{aligned} \varphi(t) &= 4\pi z(t)/\lambda \\ &= \Phi \sin \omega_A t \end{aligned} \quad (15)$$

where λ is the optical wavelength and Φ the amplitude of the phase modulation of the signal at angular frequency ω_A :

$$\Phi = 4\pi z_{max}/\lambda \quad (16)$$

Let us define the slowly varying complex amplitude $E(t)$ of the field $\mathcal{E}(t)$ scattered by the vibrating object. We have :

$$\mathcal{E}(t) = E(t)e^{j\omega_I t} + \text{c.c.} \quad (17)$$

Because of the Jacobi-Anger expansion, we get :

$$\begin{aligned} E(t) &= E e^{j\varphi(t)} = E e^{j\Phi \sin \omega_A t} \\ &= E \sum_m J_m(\Phi) e^{jn\omega_A t} \end{aligned}$$

where E is the complex amplitude without vibration, and J_m the m th-order Bessel function of the first kind, with $J_{-m}(z) = -1^m J_m(z)$ for integer m and real z . The scattered field $\mathcal{E}(t)$ is then the sum of the carrier and sideband field components $\mathcal{E}_m(t)$ of frequency ω_m , where m is the sideband index with :

$$\begin{aligned} \mathcal{E}(t) &= \sum_{m=-\infty}^{+\infty} \mathcal{E}_m(t) \\ \mathcal{E}_m(t) &= E_m e^{j\omega_m t} + E_m^* e^{-j\omega_m t} \\ \omega_m &= \omega_I + m\omega_A \end{aligned} \quad (18)$$

where E_m is the complex amplitude of the field component $\mathcal{E}_m(t)$. Note that $\omega_0 = \omega_I$ is the illumination optical frequency. Equation 18 yields :

$$E_m = J_m(\Phi) E \quad (19)$$

Figure 8 presents the distribution of the field energy on the sidebands components $|E_m|^2$ for $\Phi = 0.3$ and $\Phi = 3$. If the amplitude of modulation Φ is low (see Fig. 8 (a)), most of the energy is on the carrier : $|E_0|/|E|^2 \simeq 1$, and energy $|E_m|^2$ decreases rapidly with the sideband index m . If the amplitude Φ is large (see Fig. 8 (b)), the energy of the carrier is low : $|E_0|/|E|^2 \ll 1$, while energy is distributed over many sidebands $|E_m|^2$.

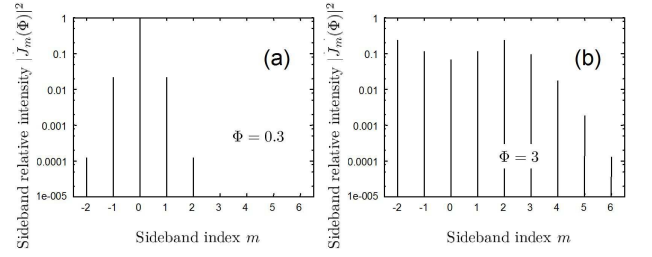


FIGURE 8. Relative amplitude $|E_m|^2/|E|^2 = |J_m(\Phi)|^2$ of the sideband component m for an amplitude modulation of the phase equal to $\Phi = 0.3$ (a) and $\Phi = 3.0$ (b) rad.

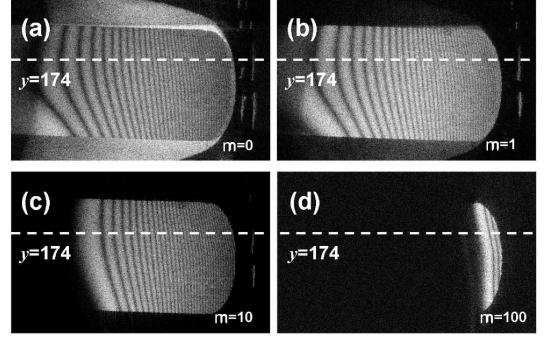


FIGURE 9. Reconstructed holographic images of a clarinet reed vibrating at frequency $\omega_A/2\pi = 2143$ Hz perpendicularly to the plane of the figure. Figure (a) shows the carrier image obtained for $m = 0$. Fig. (b)-(d) show the frequency sideband images respectively for $m = 1$, $m = 10$, and $m = 100$. A logarithmic grey scale has been used. See [13].

B. Selective detection of the sideband components E_m : by sideband holography [13]

Heterodyne holography is well suited to detect the vibration sideband components E_m . To selectively detect by four phase demodulation the sideband m of frequency ω_m , the frequency, ω_{LO} must be adjusted to fulfill the condition :

$$\begin{aligned} \omega_{LO} &= \omega_I + m\omega_A + \omega_{CCD}/4 \\ &= \omega_m + \omega_{CCD}/4 \end{aligned} \quad (20)$$

$$\text{with } \omega_m = \omega_I + m\omega_A$$

Figure 9 shows images obtained by detecting different sideband m of a clarinet reed [13]. The clarinet reed is attached to a clarinet mouthpiece and its vibration is driven by a sound wave propagating inside the mouthpiece, as in playing conditions, but the sound wave is created by a loudspeaker excited at frequency ω_A and has a lower intensity than inside a clarinet. The excitation frequency is adjusted to be resonant with the first flexion mode (2143 Hz) of the reed.

Figure 9 (a) is obtained at the unshifted carrier frequency ω_0 . It corresponds to an image obtained by time



FIGURE 10. Clarinet reed reconstructed images obtained on sideband $m = 1$. Frequency ω_A is swept from 1.4 KHz up to 20 KHz, and images are displayed from left to right and top to bottom (26×7 images). The display is made with arbitrary grey scale for the intensity $|E_0(x, y)|^2$. See [21].

averaging holography [14]. The left side of the reed is attached to the mouthpiece, and the amplitude of vibration is larger at the tip of the reed on the right side; in this region the fringes become closer and closer and difficult to count. The mouthpiece is also visible, but without fringes since it does not vibrate.

Similar images of vibrating objects have been obtained in [15–20], with more conventional techniques performing the holographic detection at the illumination frequency (i.e. carrier frequency). The quality of the images obtained in [15–20] are generally lower. Indeed, single frame holography is used in [15–20]. The total amount of signal is thus lower. Moreover, single frame holography is unable to filter off the LO beam noise by making difference of images. The technical noise and the order zero alias are much bigger as discussed in [12].

Figures 9 (b) to (d) show images obtained for the sidebands $m = 1, 10$ and 100 . As expected, the non-vibrating mouthpiece is no longer visible. Figure 9 (b) shows the $m = 1$ sideband image, with J_1 fringes that are slightly shifted with respect to those of J_0 . Figure 9 (c) shows the image of sideband $m = 10$ and Fig. 9 (d) the $m = 100$ one. The left side region of the image remains dark because, in that region, the vibration amplitude is not sufficient to generate these sidebands, $J_m(z)$ being evanescent for $z < m$.

In a typical heterodyne holography setup, RF generators drive AOM1 and AOM2 at ω_{AOM1} and ω_{AOM2} , the camera at ω_{CCD} , and the vibration frequency at ω_A . These generators use a common 10 MHz reference frequency, and are driven by the computer. It is then possible to automatically sweep ω_A , ω_{AOM1} and ω_{AOM2} in order to fulfil Eq. 20 so that detection remains ever tuned on a given sideband. Figure 10 shows an example [21]. A series of 26×7 images of a clarinet reed are obtained on

sideband $m = 1$ by sweeping the frequency ω_A from 1.4 kHz up to 20 kHz by steps of 25 per cents (factor 1, 1.25, $(1.25)^2$, $(1.25)^3$...). The amplitude of the excitation signal is exponentially increased in the range 1.4 to 4 kHz, from 0.5 to 16 V, then kept constant at 16 V up to 20 kHz. This crescendo limits the amplitude of vibration of the first two resonances of the reed. The different vibration modes of the reed can be easily recognized on the reconstructed reed images of Fig. 10.

Sideband heterodyne holography is a very powerful technique, which has been used to image objects whose vibration amplitude are both large [22] and small [23–27]. Combined with stroboscopic illumination/detection [28] or with sideband correlation analysis [29], sideband heterodyne holography has been made sensitive to the phase of the vibration.

C. Analyse of Doppler spectrum of light that travel through the breast [30]

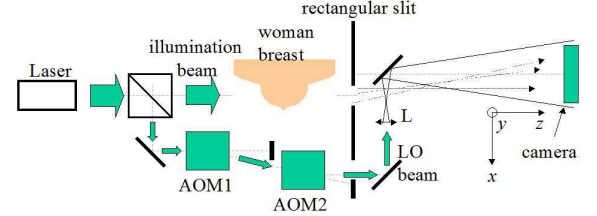


FIGURE 11. Doppler spectrum experimental setup. BS : beam splitter; AOM1, AOM2 : acousto optic modulator; L : short focal lens. Laser : near infrared laser (70 mW, 780 nm).

The purpose of the second example of experiment is to measure the spectral broadening of the light that travel through a woman breast in vivo. This experiment has been made in the context of ultrasonic photon tagging [31–35], whose purpose is to detect breast cancer. In that context the measure of the light spectral broadening, which is related to the breast transmitted light correlation time is important, since light decorrelation is important limitation of the performance of the ultrasonic photon tagging method.

Figure 11 shows the heterodyne holography experimental setup. The object, whose image is reconstructed by holography, is a rectangular slit that is back illuminated by laser beam (70 mW, 780 nm) that travel through the breast. The position of the lens L is adjusted so that the LO beam reach the camera off axis with respect to the object (the slit). Moreover, the slit to camera distance is made equal to the radius of curvature of the LO beam that reach the camera. By this way, the reconstruction of the $+1$ and -1 grating order images of the slit are made by a simple Fourier transform.

Figure 12 (a) shows the four frames Fourier space hologram $|\tilde{H}|^2$ that was obtained for $\omega_{AOM1} = \omega_{AOM2}$ i.e.

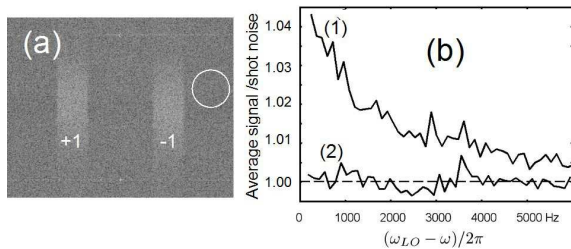


FIGURE 12. (a) Four frames Fourier space hologram $|\tilde{H}|^2$ obtained in the breast experiment for $\omega_{LO} = \omega_I$. Display is made in arbitrary logarithmic gray scale. (b) Ratio of $|\tilde{H}|^2$ averaged within the +1 and -1 images of the slot, versus $|\tilde{H}|^2$ averaged within the white circle quiet zone, as a function of $(\omega_{LO} - \omega_I)/2\pi$ (curve 1) and $(\omega_{LO} - \omega_I)/2\pi + 100$ kHz (curve 2).

for $\omega_{LO} = \omega_I$. The two brighter vertical bands are the +1 and -1 grating order images of the slit, which are both on focus because of the peculiar location of lens L. The +1 image corresponds to the $|E|^2$ signal at frequency $\omega_{LO} + \omega_{CCD}/4$, while the -1 image corresponds to $\omega_{LO} - \omega_{CCD}/4$.

Because the breast inner motions are random, the frequency spectrum of the light scattered by breast is continuously broadened. In that spectrum the 4 phases detection that is made here selects the signal at frequency $\omega_{LO} + \omega_{CCD}/4$ within the +1 image, and the signal at $\omega_{LO} - \omega_{CCD}/4$ within the -1 image. Both signals are non zero because the spectrum is continuous. Note that it is also possible to analyse the same data by making 2 phases detection with $H = I_1 - I_2$. In that case, H is a real quantity and the +1 and -1 images are both present too.

The detected signal (i.e. the brightness of slit images) is low for the following reasons.

- Most of the incoming illumination light is back reflected because the breast is highly diffusing.
- The transmitted light is scattered in all directions and few light reach the camera.
- The light that reach the camera is Doppler broadened by the breast inner motions. Since this Doppler broadening is large with respect to the heterodyne detection bandwidth $BW = (4NT)^{-1}$, most of the light that reach the camera is not detected.

To explore the Doppler profile of the scattered photons, the frequency of the LO beam offset $(\omega_{LO} - \omega_I)/2\pi$, was swept from 0 Hz up to 5000 Hz. To obtain a better signal, the 4 frames holograms $|\tilde{H}|^2$ have been averaged over 32

sequences of four frames. We have then measured the averaged signal within both the +1 and -1 images of the slit, and compared this signal with the averaged signal in a quiet zone of the Fourier space, like the zone within the white circle in the right of Fig. 12 (a). The signal, within the quiet zone, corresponds to shot noise i.e. to 1 e per pixel.

We have plot, on Fig. 12 (b) (curve 1), the ratio of the averaged +1 and -1 signal $|\tilde{H}|^2$, versus the averaged signal within the quiet zone, as a function of $(\omega_{LO} - \omega_I)/2\pi$ (curve 1). Because of the ratio, the vertical scale is the averaged signal $|E|^2$ in photo electron Units. In order to better visualise the background noise, we have also plotted on Fig. 12 (b) (curve 2), the ratio versus $(\omega_{LO} - \omega_I)/2\pi + 100$ KHz. Since 100 KHz is much larger than the half width of Doppler spectrum (about 1.5 kHz), curve 2 corresponds to the background noise, that is effectively equal to shot noise, i.e., 1 e .

This last experiment shows how it is possible to explore a Doppler spectrum by heterodyne holography. It illustrates also the sensitivity of Doppler holography, since the signal that is analyzed is very low : $|E|^2$ very less than 0.05 e at maximum.

The Doppler heterodyne holography method, that is illustrated here, has been used in many other contexts. The method has been used to detect the tagged photons in ultrasonic photon tagging experiments [4], to study brownian motion effects in coherent back scattering [36], and to image blood flow, in mouse crania [37, 38], rat eye [39] and fish embryo [8].

IV. CONCLUSION

In this paper, we have presented the digital heterodyne holography technique that is able to fully control the amplitude, phase and frequency of both illumination and reference beams. This control is made by acousto optic modulator, which are driven electronically by RF generators. Heterodyne holography is an extremely versatile and powerful tool, able to perform automatic data acquisition in any holographic configuration with accurate phase and shot noise sensitivity.

Heterodyne holography is also able to perform the holographic detection at frequencies that are different than the illumination one. This capability is especially useful for vibration analysis, and for laser Doppler full field measurement.

We acknowledge ANR Blanc Simi 10 (n 11 BS10 015 02) grant, ANR Blanc Simi 4 (n. 11-BS04 017 04) and Labex Numev (convention ANR-10-LABX-20) grant for funding.

- experiment in the visible with on-axis digital heterodyne holography. *Opt. Lett.*, 26(20) :1550–1552, 2001.
- [3] I. Yamaguchi and T. Zhang. Phase-shifting digital holography. *Opt. Lett.*, 22(16) :1268–1270, 1997.
 - [4] M. Gross, P. Goy, and M. Al-Koussa. Shot-noise detection of ultrasound-tagged photons in ultrasound-modulated optical imaging. *Opt. Lett.*, 28(24) :2482–2484, 2003.
 - [5] T.C Poon. Optical scanning holography-a review of recent progress. *J. Opt. Soc. Korea* 13(4) : 406–415, 2009.
 - [6] N. Warnasooriya, F. Joud, P. Bun, G. Tessier, M. Coppey-Moisán, P. Desbiolles, M. Atlan, M. Abboud, and M. Gross. Imaging gold nanoparticles in living cell environments using heterodyne digital holographic microscopy. *Opt. Express*, 18(4) :3264–3273, 2010.
 - [7] F. Verpillat, F. Joud, P. Desbiolles, and M. Gross. Dark-field digital holographic microscopy for 3d-tracking of gold nanoparticles. *Opt. Express*, 19(27) :26044–26055, 2011.
 - [8] N. Verrier, D. Alexandre, and M. Gross. Laser doppler holographic microscopy in transmission : application to fish embryo imaging. *Opt. Express*, 22(8) :9368–9379, 2014.
 - [9] M. Atlan, M. Gross, and E. Absil. Accurate phase-shifting digital interferometry. *Opt. Lett.*, 32(11) :1456–1458, 2007.
 - [10] E. Cuche, P. Marquet, and C. Depeursinge. Spatial filtering for zero-order and twin-image elimination in digital off-axis holography. *Appl. Opt.*, 39(23) :4070–4075, 2000.
 - [11] F. Verpillat, F. Joud, M. Atlan, and M. Gross. Digital holography at shot noise level. *J. of Disp. Technology*, 6(10) :455–464, 2010.
 - [12] M. Gross, M. Atlan, and E. Absil. Noise and aliases in off-axis and phase-shifting holography. *Appl. Opt.*, 47(11) :1757–1766, 2008.
 - [13] F. Joud, F. Laloë, M. Atlan, J. Hare, and M. Gross. Imaging a vibrating object by sideband digital holography. *Opt. Express*, 17(4) :2774–2779, 2009.
 - [14] P. Picart, J. Leval, D. Mounier, and S. Gougeon. Time-averaged digital holography. *Opt. Lett.*, 28(20) :1900–1902, 2003.
 - [15] N. Demoli and D. Vukicevic. Detection of hidden stationary deformations of vibrating surfaces by use of time-averaged digital holographic interferometry. *Opt. Lett.*, 29(20) :2423–2425, 2004.
 - [16] N. Demoli and I. Demoli. Dynamic modal characterization of musical instruments using digital holography. *Opt. express* 13(13) : 4812–4817, 2005.
 - [17] P. Picart, J. Leval, D. Mounier, and S. Gougeon. Some opportunities for vibration analysis with time averaging in digital fresnel holography. *Appl. Opt.*, 44(3) :337–343, 2005.
 - [18] P. Picart, J. Leval, J.C. Pascal, J.P. Boileau, M. Grill, J.M. Breteau, B. Gautier, and S. Gillet. 2d full field vibration analysis with multiplexed digital holograms. *Opt. Express*, 13(22) :8882–8892, 2005.
 - [19] J. Leval, P. Picart, J. P. Boileau, and J. C. Pascal. Full-field vibrometry with digital fresnel holography. *Appl. Opt.*, 44(27) :5763–5772, 2005.
 - [20] P. Picart, J. Leval, F. Piquet, J.P. Boileau, T. Guimezanes and J. P. Dalmont Study of the Mechanical Behaviour of a Clarinet Reed Under Forced and Auto-oscillations With Digital Fresnel Holography. *Strain*, 46(1) :89–100, 2010
 - [21] P. A. Taillard, F. Laloë, M. Gross, J. P. Dalmont, and J. Kergomard. Statistical estimation of mechanical parameters of clarinet reeds using experimental and numerical approaches. *Acta Acustica united with Acustica*, 100(3) :555–573, 2014.
 - [22] F. Joud, F. Verpillat, F. Laloë, M. Atlan, J. Hare, and M. Gross. Fringe-free holographic measurements of large-amplitude vibrations. *Opt. Lett.*, 34(23) :3698–3700, 2009.
 - [23] P. Psota, V. Lédl, R. Doleček, J. Erhart, and V. Kopecký. Measurement of piezoelectric transformer vibrations by digital holography. *IEEE Transactions on Ultrasonics, Ferroelectrics and Frequency Control*, 59(9) :1962–1968, 2012.
 - [24] P. Psota, V. Lédl, R. Doleček, J. Václavík, and M. Šulc. Comparison of digital holographic method for very small amplitudes measurement with single point laser interferometer and laser doppler vibrometer. In *Digital Holography and Three-Dimensional Imaging*, pages DSu5B–3. OSA, 2012.
 - [25] N. Verrier and M. Atlan. Absolute measurement of small-amplitude vibrations by time-averaged heterodyne holography with a dual local oscillator. *Opt. Lett.*, 38(5) :739–741, 2013.
 - [26] F. Bruno, J. Laurent, D. Royer, and M. Atlan. Holographic imaging of surface acoustic waves. *Appl. Phys. Lett.*, 104(8) :083504, 2014.
 - [27] P. Psota, V. Lédl, and R. Doleček. High dynamic range digital holographic method for very small amplitude measurement. In *Fringe 2013*, pages 635–640. Springer, 2014.
 - [28] F. Verpillat, F. Joud, M. Atlan, and M. Gross. Imaging velocities of a vibrating object by stroboscopic sideband holography. *Opt. Express*, 20(20) :22860–22871, 2012.
 - [29] N. Verrier, L. Alloul, and M. Gross. Vibration of low amplitude imaged in amplitude and phase by sideband versus carrier correlation digital holography. *Opt. Lett.*, 40(3) :411–414, 2015.
 - [30] M. Gross, P. Goy, B. C. Forget, M. Atlan, F. Ramaz, A. C. Boccara, and A. K. Dunn. Heterodyne detection of multiply scattered monochromatic light with a multipixel detector. *Opt. Lett.*, 30(11) :1357–1359, 2005.
 - [31] W. Leutz and G. Maret. Ultrasonic modulation of multiply scattered light. *Physica B : Condensed Matter*, 204(1) :14–19, 1995.
 - [32] L. Wang, S. L. Jacques, and X. Zhao. Continuous-wave ultrasonic modulation of scattered laser light to image objects in turbid media. *Opt. Lett.*, 20(6) :629–631, 1995.
 - [33] S. Leveque, A.C. Boccara, M. Lebec, and H. Saint-Jalmes. Ultrasonic tagging of photon paths in scattering media : parallel speckle modulation processing. *Opt. Lett.*, 24(3) :181–183, 1999.
 - [34] T. W. Murray, L. Sui, G. Maguluri, R. A. Roy, A. Nieva, F. Blonigen, and C. A. DiMarzio. Detection of ultrasound-modulated photons in diffuse media using the photorefractive effect. *Opt. Lett.*, 29(21) :2509–2511, 2004.
 - [35] F. Ramaz, B. C. Forget, M. Atlan, A. C. Boccara, M. Gross, P. Delaye, and G. Roosen. Photorefractive detection of tagged photons in ultrasound modulated optical tomography of thick biological tissues. *Opt. Express*, 12(22) :5469–5474, 2004.
 - [36] M. Lesaffre, M. Atlan, and M. Gross. Effect of the photon’s brownian doppler shift on the weak-localization coherent-backscattering cone. *Phys. Rev.*

- Lett.*, 97(3) :033901, 2006.
- [37] M. Atlan, M. Gross, B. C. Forget, T. Vitalis, A. Rancillac, and A. K. Dunn. Frequency-domain wide-field laser doppler in vivo imaging. *Opt. Lett.*, 31(18) :2762–2764, 2006.
- [38] M. Atlan, B. C. Forget, A. C. Boccara, T. Vitalis, A. Rancillac, A. K. Dunn, and M. Gross. Cortical blood flow assessment with frequency-domain laser doppler microscopy. *J. of Biomed. Opt.*, 12(2) :024019–024019, 2007.
- [39] M. Simonutti, M. Paques, J. A. Sahel, M. Gross, B. Samson, C. Magnain, and M. Atlan. Holographic laser doppler ophthalmoscopy. *Opt. Lett.*, 35(12) :1941–1943, 2010.